AGU100 ADVANCING EARTH AND SPACE SCIENCE

Water Resources Research

RESEARCH ARTICLE
10.1029/2018WR022782

Key Points:
- The 2-D velocity fields around a scaled unban drainage inlet grate are measured using a surface PIV system and compared to numerical simulations
- The comparison shows higher inflows in the experimental results due to a localized transition from weir to orifice condition near the void areas of the grates
- The work demonstrates the potential for further use of 2-D models to describe flow conditions at a range of urban drainage linking elements

Correspondence to:
R. Martins,
ricardo.martins@sheffield.ac.uk

Citation:
Martins, R., Rubinato, M., Kesserwani, G., Leandro, J., Djordjević, S., & Shucksmith, J. D. (2018). On the characteristics of velocities fields in the vicinity of manhole inlet grates during flood events. *Water Resources Research*, *54*. https://doi.org/10.1029/2018WR022782

Received 16 FEB 2018
Accepted 30 JUL 2018
Accepted article online 8 AUG 2018

On the Characteristics of Velocities Fields in the Vicinity of Manhole Inlet Grates During Flood Events

R. Martins[1,2], M. Rubinato[1], G. Kesserwani[1], J. Leandro[3,4,5], S. Djordjević[6], and J. D. Shucksmith[1]

[1]Department of Civil and Structural Engineering, Mappin Building, S1 3JD The University of Sheffield, Sheffield, UK, [2]Earth Surface Process Team, Centre for Environmental and Marine Studies (CESAM), Department of Environment and Planning, University of Aveiro, Aveiro, Portugal, [3]Department of Civil, Geo and Environmental Engineering, Chair of Hydrology and River Basin Management, Technical University of Munich, Munich, Germany, [4]Marine and Environmental Sciences Centre, Department of Civil Engineering, FCT, University of Coimbra, Coimbra, Portugal, [5]Institute of Marine Research, FCT, University of Coimbra, Coimbra, Portugal, [6]Centre for Water Systems, University of Exeter, Exeter, UK

Abstract The accurate characterization of flow from urban surfaces to sewer/stormwater systems is important for urban drainage design and flood modeling/risk identification. However, the geometrical complexity and large variety of drainage structures (linking elements) available makes model calibration and verification difficult. In this study an extensive comparison between experimentally measured and numerically modeled flow characteristics in the vicinity of ten different designs of manhole grate was performed under drainage flow in subcritical conditions. Using a 2-D surface PIV (sPIV) system the work presents the first detailed characterization of velocity fields around these linking elements. In addition, it provides the first detailed verification of the ability of a 2-D numerical model to describe both velocity fields and drainage flows. The overall comparison shows a close relationship between numerical and the experimental results with some higher inflows in the experimental results as a consequence of a localized transition from weir to orifice condition near the void areas of the grates. It was also noted that velocity differences decreased further from the manhole, due mainly to the more directional flow. Overall the work demonstrates the potential for further use of 2-D numerical models to describe flow conditions at linking elements, either directly within modeling simulations or indirectly via the characterization of energy loss coefficients.

1. Introduction

Pluvial flooding events lead to interactions between overland surface flow and surcharged sewer flows at interface linking drainage structures such as gullies and manholes. These events can lead to heavy monetary and social losses. These events can be caused or exacerbated by a lack of capacity of the urban drainage system to convey stormflows, or a lack of capacity of urban drainage linking elements to transfer flows from surface to drainage systems. Efficient drainage of urban environments is of the utmost importance and one of the major critical services provided to the citizens (Yang et al., 2017). Storm water management infrastructure plays a very important role in the hydrological response (Yang et al., 2016). As such, understanding and characterizing the flows at such linking elements is therefore critical for urban design and flood risk assessment. The urban drainage system is composed of two systems, the major and the minor systems (Nasello & Tucciarelli, 2005). The major system, which is composed of the surface flow conveying system (pathways and watercourses), is usually modeled as a network of 1-D channels, a full 2-D area, or the combination of 1-D network and 2-D ponds. Full 2-D models usually rely on the nonlinear shallow water equations or some of its simplifications. These equations are usually applied to several flows (Chertock et al., 2015) and are obtained from the Navier-Stokes equations assuming an inviscid, isothermal, and incompressible flow with an hydrostatic pressure distribution. The minor system, the enclosed drainage system, conveys the flow underground or through enclosed structures to remove the water from the affected areas, is usually modeled through a network of 1-D surchargeable pipes, culverts, or small watercourses. The connection between both systems is made through a linkage, which includes the urban drainage linking elements such as gullies, manholes, and gutters, and is usually modeled as a calibratable single weir/orifice equation (Martins, Leandro, Chen, et al., 2017) as a simplification. The accuracy of such a simplification is dependent on the appropriate determination of both an energy loss coefficient, as well as the prevailing

hydraulic head within the linkage structure (Rubinato et al., 2017). One of the major complexities when modeling dual drainage (i.e., drainage and surcharge) is verifying if the flow and head around linking structure is being correctly represented in the model and that the flow drained into the minor system is well represented by such simplifications.

Studies on linkage systems are usually focused on experimental facilities with emphasis on the efficiency (Bock et al., 1956; Gómez & Russo, 2009; Gómez & Russo, 2011; Li, Geyer, et al., 1951; Li, Sorteberg, et al., 1951; Li et al., 1954a, 1954b; Martins et al., 2014; Russo et al., 2013) or the use of fully 3-D CFD models to study the characteristics of the flow inside the manhole (Djordjevic et al., 2013; Leandro et al., 2014; Lopes et al., 2015, 2016). Studies that verify the applicability of 2-D models to directly reproduce drainage flows and flow conditions close to the linkage structure on the floodplain during flood events are however scarce (Martins, Kesserwani, et al., 2017; Rubinato et al., 2018), and proper validation is usually focused on the bed elevation (Cea et al., 2014) far from the interface structures.

Bock et al. (1956); Li, Geyer, et al. (1951); Li et al. (1954a, 1954b); and Li, Sorteberg, et al. (1951) performed a series of studies focusing on the characteristics of flows entering gullies with varying geometric properties presenting formulas to calculate the capacity of generic longitudinal grate with no street depression, for kerb-opening inlets with and without standard depression, for oblique (deflector inlets) grates in gullies varying the degree, and for the combination of gullies with longitudinal and perpendicular openings and kerb-opening inlets, concluding with a methodology to compute the capacity of combination of standard inlets. These studies however consider the flow on the surface based on an assumed flow that starts parallel to the direction of the grate and then follows a curve inside the grates splitting the flow in carry-over discharge past the inlet and carry-over discharge between the curb and the grate.

Spaliviero et al. (2000) analyzed six types of grate geometries and proposed a predictive method to obtain the efficiency of the flow through gratings, once more based on the theoretical flow on the surface. Gómez and Russo (2005, 2007, 2009, 2011) performed a series of tests mainly to check the efficiency of inlets, based on experimental data. Russo et al. (2013) and Lopes et al. (2016) analyzed experimentally and numerically the efficiency of several continuous transverse grates reaching the conclusion that a 3-D VOF model can effectively replicate the efficiency of a grate.

Djordjevic et al. (2013) performed a study on the surface and subsurface interaction presenting results for drainage and surcharge of a grated gully with transversal voids. They used a 3-D and a 2-D localized surface model varying the transversal slope for a common gully in the UK. Leandro et al. (2014), Martins et al. (2014), and Lopes et al. (2015) focused on a traditional gully and characterized numerically and experimentally the flow inside a manhole using velocity profiles and free surface for the surcharge situation, and coefficients for the drainage. However, the study was limited to fully open manholes with no consideration of the effects of a grated inlet.

From the literature it is noteworthy that the main focus of existing studies is bulk flow rates through single gullies or kerb openings, either via highly empirical efficiency relationships or 3-D CFD studies. Such studies are highly site-specific, time intensive, and/or difficult to implement with existing 1-D–2-D flood model architecture. Verification studies are based on depth and flow rates, which do not capture the fully hydraulic complexity of flows around such linking elements in drainage conditions.

Therefore, this work presents formal testing and validation of a fully dynamic model based on the 2-D shallow water equations performed near the vicinity of a manhole inlet during shallow subcritical drainage conditions. Several different grate inlets are considered over a range of steady shallow flow depths. A detailed comparison between experimental and numerical results including 2-D velocity fields in the vicinity of the grates (collected experimentally using a large scale surface PIV system) as well as drainage flows are presented. The overall objective is to provide improved understanding of the behavior of velocity fields around manhole grates through a physical-scaled modeling study and use this new data to validate the ability of 2-D depth-averaged hydrodynamic models to simulate such complex flows.

2. Methodology

Experimental testing to characterize steady drainage flows were conducted using a scaled (1:6) physical model of a linked sewer/surface system constructed at the University of Sheffield (Figure 1). The model is composed of an 8.2-m-long, 4-m-wide surface "floodplain" constructed from acrylic (slope of 0.001 m/m).

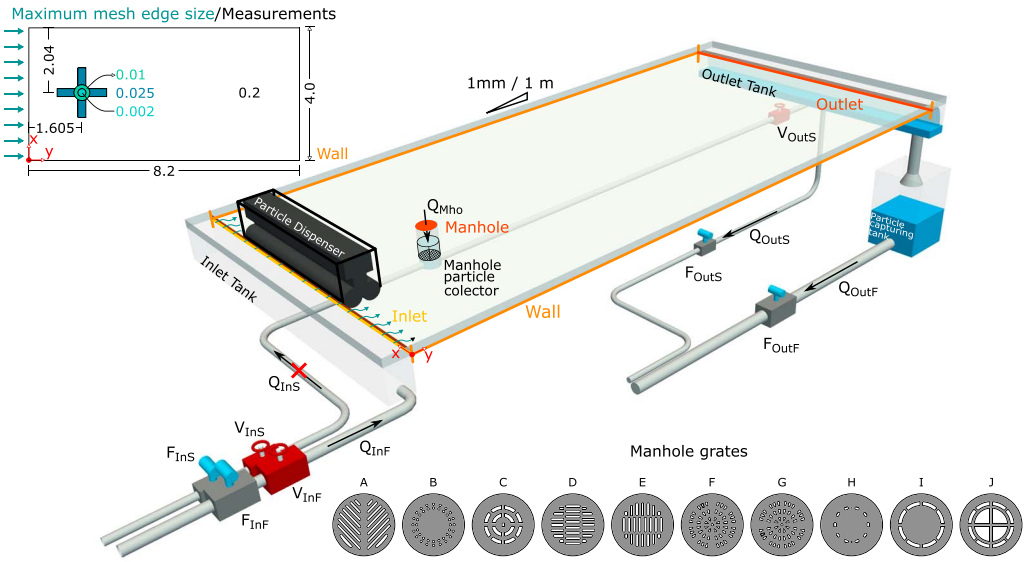

Figure 1. The 3-D representation of the experimental facility, mesh dimension (top left corner), and inflow details. All dimensions in meters.

This is connected to a piped sewer system via a manhole with a diameter of 0.240 m (simulating a 1.440-m manhole at full scale, a size typical of UK urban drainage systems for pipes diameters up to 900 mm; DEFRA, 2011). The sewer comprises a 0.075 m (internal) diameter clear acrylic pipe (simulating a 0.450-m pipe at full scale). To simulate drainage conditions a series of steady flows were passed over the inlet weir at the upstream boundary of the floodplain system. A portion of this flow passes into the piped drainage system via the manhole structure, with the remaining flow passing to the surface outlet tank via the downstream boundary. For the tests detailed here no inflow to the sewer system was simulated.

2.1. Grates

Experiments were conducted using eight different grate designs applied to the top of the manhole structure. Grates were designed in AutoCAD and fabricated from a sheet of acyclic using a laser cutter. The grates were designed to sit flush with the floodplain surface and were fixed in place for each experiment. The different manhole designs were based on grates found worldwide considering a range of varied geometries (Figure 1). Two of the grates (D and F) show a preferential flow direction, as such they were also tested when rotated 90° resulting in ten configurations with different geometries. Grate A also shows a nonradial symmetry; however, the grate usually is installed following the preferential direction and as such it was not tested in other directions. Several parameters have been used to characterize the static geometrical properties of the grates configuration based on the AutoCAD designs (Table 1).

The void area represents the "empty area" in each design that may allow flow into the manhole from the surface while the void perimeter represents the wetted perimeter of the void spaces. These are commonly utilized when applying the weir or orifice equation to calculate the exchange flow between the surface and the sewer system within flood models (Rubinato et al., 2017); however, in low-depth flows, the full void areas and wetted perimeter may not be fully utilized due to downstream voids being partially obstructed by those

Table 1
Geometrical Characteristics of the Manhole Grates Tested

Manhole grate	A	B	C	D	E	F	G	H	I	J
Filled area (m^2)	0.0307	0.0421	0.0373	0.0353	0.0353	0.0391	0.0391	0.0435	0.0385	0.0277
Void area (m^2)	0.0145	0.0031	0.0079	0.0099	0.0099	0.0061	0.0061	0.0017	0.0067	0.0175
Void ratio (%)	32.1	6.9	17.48	21.9	21.9	13.5	13.5	3.76	14.11	38.03
Void perimeter (m)	3.0364	1.252	1.388	2.3794	2.3794	2.2586	2.2586	0.5128	1.2428	1.8816

upstream. Due to the difficultly in accurately measuring the effective utilized wetted perimeter and void area during flow events, such low-depth conditions can represent a specific challenge to the calibration and implementation of weir/orifice flow exchange equations.

2.2. Flow Measurements

The experimental facility is equipped with three electromagnetic flowmeters (×1 at the surface flow inlet − Q_{InF}, ×2 in the outlets of the sewer and surface systems, Q_{OutS}, Q_{OutF}) of 0.075-m internal diameter. The accuracy of the flowmeters has been validated using volumetric discharge readings using the laboratory measurement tank. A butterfly flow control valve was fitted to the pipe that feeds the floodplain such that a range of steady inflows can be set. Electromagnetic flowmeters and butterfly valve are monitored and controlled via Labview™ software.

Steady state flow exchange rate through the manhole structure (Q_{Mho}) is quantified based on mass conservation principles as follows:

$$Q_{Mho} = \overline{Q_{InF}} - \overline{Q_{OutF}} = Q_{OutS} \quad (1)$$

where $\overline{Q_{InF}}$ and $\overline{Q_{OutF}}$ are the time-averaged floodplain inflow and outflow, respectively. For all the tests conducted, flows were first established and allowed to stabilize before data values were recorded. Once established, data were collected for a period of 3 min in order to define reliable temporally averaged values.

2.3. Local 2-D Velocity Measurement

In order to experimentally characterize velocity fields in the vicinity of the grate inlet a large-scale surface PIV (sPIV) system was implemented. sPIV systems are commonly used to characterize 2-D velocity fields of the flow surface over a larger measurement area than conventional PIV (Carmer et al., 2009). A GoPro Hero 4 Black Edition camera (set to record video frames of size 1,440 × 1,920 pixels, representing a total measurement area of 0.76 by 0.57 m) was fitted at a height of 1.5 m directly above the manhole inlet to acquire video frames for the application of the particle image velocimetry analysis. Based on this setup a resolution of approximately 1 mm per pixel at the center of the images was obtained with a consequent maximum frame rate of 80 Hz. This also ensured that each sPIV seeding particle (polypropylene, 2- to 3-mm diameter with density 0.90 g/cm^3; Weitbrecht et al., 2002) was represented by a cluster of at least 5 pixels, giving good particle definition and ensuring accurate detection by the PIV software (Dynamic Studio by *DantecDynamicsLtd*).

The lens distortion effect was removed from the images by dewarping the frames based on the use of a calibration chequerboard image. Pixels outside the measurement area were cropped for each image. Prior to each test the mean "background" (i.e., with no seeding particles) image was recorded over 3 min. The subsequent sPIV instantaneous images were then subtracted from this background, such that the background would turn black while the particles would remain white. Seeding particles were applied to the flow via an upstream roller brush attached to a vibrating particle hopper. Measurements were recorded for a period of 3 min for each test. After this step, these images were analyzed using the commercial PIV software Dynamic Studio and an adaptive correlation was performed to determine the velocity field for each time adjacent image pair. A range validation was applied to remove unauthentic high velocities and zero velocities resulting from interrogation areas with no seeding particles. For each flow condition the filter removed less than 5% of the velocity vectors. The velocity vectors were then replaced via a 3 × 3 moving time average routine. This technique averages velocity values around the rejected areas to generate final replacement values.

2.4. Hydraulic Testing Conditions

For each inlet grate, a range of eight different steady surface flow rates were tested. The drainage (exchange) flow and velocity fields were characterized for each test conducted. Flow depths were measured 300 mm upstream of the manhole and were influenced by both flow rates as well as the different manhole grids (due to different backwater effects). The measured flow depths ranged between 7.0 and 15.0 mm over the tests conducted, with calculated mean primary surface flow velocities in the range 0.1–0.250 ms^{-1}. Flow Reynolds numbers were in the range of 1,050–2,500, and hence can be considered sufficient to avoid significant viscosity effects (Tracy, 1957). Froude numbers were in the range 0.495–0.612, and hence, all the flows replicated are under subcritical conditions. Scaling by Froude similitude based on equivalent flow depths over a full-size grate results in surface flow velocities in the range of 0.25–0.625 ms^{-1}, which may be

considered representative of urban surface flood flow over shallow slopes (Djordjevic et al., 2013; Odzemir et al., 2013). Table 2 presents mean measured total inflow rates ($\overline{Q_{InF}}$) together with minimum and maximum Froude and Reynolds Nos upstream of the manhole over all tested grates tested.

2.5. Numerical Model

The numerical simulations were conducted using a finite volume method to obtain velocities in the vicinity of the manhole. The shallow water equations (SWEs) were used as they are the mostly used equations to simulate urban flood events. The 2-D SWE are represented by three partial differential equations:

$$\frac{\partial h}{\partial t}+\frac{\partial q}{\partial x}+\frac{\partial p}{\partial y}=0 \tag{2}$$

$$\frac{\partial q}{\partial t}+\frac{\partial q^2h^{-1}}{\partial x}+\frac{g}{2}\frac{\partial h^2}{\partial x}+\frac{\partial qph^{-1}}{\partial y}=gh\frac{\partial B(x,y)}{\partial x}+\tau_{bx} \tag{3}$$

$$\frac{\partial p}{\partial t}+\frac{\partial qph^{-1}}{\partial x}+\frac{\partial p^2h^{-1}}{\partial y}+\frac{g}{2}\frac{\partial h^2}{\partial y}=gh\frac{\partial B(x,y)}{\partial y}+\tau_{by} \tag{4}$$

Equation (2) is the mass conservation equation, with h the water depth, q the momentum in the x direction, p in the y direction, and t the time. Equations (3) and (4) are the momentum conservation equations, where $B(x,y)$ is the generic function for the topography elevation, τ_{bx} is the bed friction stress in the x direction, and τ_{by} is the bed friction stress in the y direction.

2.5.1. Roe Riemann Solver on Unstructured Mesh

A finite volume Godunov method is used to integrate the 2-D equations (equations (2), (3), and (4)) on a 2-D unstructured node-centered triangular mesh. The numerical fluxes are computed using a well-balanced upwind Roe Riemann Solver (Martins et al., 2015) suitable for flood modeling. Bed friction is computed using a semi-implicit point-wise scheme (Song et al., 2011) by redefining the velocities as

$$\begin{bmatrix}u^{t+1}\\v^{t+1}\end{bmatrix}=(1+\Delta t\zeta_u)^{-1}\begin{bmatrix}u^{t}\\v^{t}\end{bmatrix},\ with\ \zeta_U=gn^2h^{-4/3}\|U\| \tag{5}$$

where U is the velocity vector with components $u=ph^{-1}$ and $v=qh^{-1}$ in the x and y directions, respectively; Δt is the time step; g is the gravitational constant; and n is the Manning's roughness coefficient (taken as 0.011 $sm^{-1/3}$ based on the bed material). Wetting and drying was computed based on the flux restricting numerical treatment presented in Martins, Leandro, and Djordjevic (2017). The spatial and temporal integrations are first order with time step increment controlled by the CFL condition with a Cr no. = 1 (Martins et al., 2015). First-order accuracy was deemed accurate enough as the approximate steady state did not require an increase in the numerical model's precision.

2.5.2. Boundary and Initial Conditions

Four boundary conditions were considered for this work as presented in Figure 1. Two walls exist parallel to the flow at $x=0$ m and $x=4$ m. The numerical boundary condition considered is a fully reflective boundary including wall friction. This is obtained by increasing the area in the friction loss term τ_{bx} and τ_{by}. As such, and following the same approach as Molls et al. (1998) for structured meshes and Brufau and García-Navarro (2000) for cell-centered unstructured meshes, the ζ_u term is redefined as

$$\zeta_U=g\left(n^{\frac{3}{2}}h^{-1}\begin{bmatrix}1&0\\0&1\end{bmatrix}+n_w^{\frac{3}{2}}A_{nw}^{-1}\begin{bmatrix}l_{nwx}&0\\0&l_{nwy}\end{bmatrix}\right)^{4/3}\|U\| \tag{6}$$

where n_w is the equivalent Manning's roughness coefficient for the wall, herein considered the same as the bed since the material is the same; l_{nwx} and l_{nwy} are the total length of wall projected to the x and y Cartesian directions, respectively; and A_{nw} is the computational cell area.

The inlet velocity was obtained by performing ten measurements of velocity using the sPIV system for ten different floodplain inflows (from 2.75 to 10 L/s) every 0.5 m perpendicular to the inlet weir. These

Table 2
Mean Inflow Rates ($\overline{Q_{InF}}$), Depth, Froude, and Reynolds Number Upstream of the Manhole for Each Upstream Valve Opening (R###) (Rubinato, 2015)

	R120	R125	R130	R135	R140	R145	R150	R160
Inflow (L/s)	4.27	4.97	5.66	6.30	6.93	7.52	8.19	9.24
Depth (mm)	7.3–7.7	7.8–8.4	8.5–9.2	9.1–10.1	9.5–10.7	9.7–11.2	10.6–11.7	11.4–12.5
Froude number (–)	0.50–0.56	0.51–0.57	0.51–0.58	0.49–0.58	0.50–0.60	0.51–0.59	0.52–0.60	0.53–0.61
Reynolds number (–)	1052–1080	1230–1247	1404–1421	1562–1588	1714–1738	1736–1882	2035–2050	2299–2318

measurements were averaged for each position and for each flow. It can be observed that the inflow velocity is not fully uniform over the width of the flume. Because of the variable velocity, and to simplify the implementation of the velocities in the numerical model, the fourth-order algebraic equation (7) was fitted to the averaged flow as shown in Figure 2a:

$$\overline{V_{InF}} = \begin{bmatrix} 1.71\times10^{-4} \\ -2.72\times10^{-3} \\ 1.13\times10^{-3} \\ 1.71\times10^{-1} \end{bmatrix} \begin{bmatrix} Q_{InF}^4 & Q_{InF}^3 & Q_{InF}^2 & Q_{InF} \end{bmatrix} \quad (7)$$

The velocities were also averaged position-wise and normalized to obtain a spatial distribution along the inlet (x) axis (Figure 2b and a regular boundary condition. Since the mesh at the inlet is different for each grate, the inlet velocities were divided space-wise in five positions ([0,0.1[, [0.1,1.75[, [1.75,2.25],]2.25,3.9],]3.9,4]) and averaged over each length, resulting in the coefficients (0,1.051,0.89,0.986,0) that are to be used to increase or reduce the average velocity.

Since the floodplain flow is subcritical, critical flow boundary condition is imposed to separate the mesh and the void spaces at the grates. It should be noticed that the flow through these sort of grates is of very high complexity as the "used" perimeter/area changes with depth and flow and the transition from weir to orifice is not straightforward. Therefore, to simplify and test the numerical procedure a critical flow with free exit was used as the void boundary condition.

Since the floodplain is long enough without perturbations after the manhole, the uniform depth calculated for a rectangular channel was assumed correct and used in the outlet downstream boundary at each time step.

2.5.3. Domain Discretization

The mesh was tailored to each grate and a finer mesh was used where required to improve the accuracy of the model diminishing the small differences between meshes. The maximum edge size for the mesh was based on previous studies (Martins, Kesserwani, et al., 2017; Rubinato et al., 2017) being 0.002 m inside the manhole area ($r < 0.12$ m), 0.01 m in the outer circle (0.12 m $< r <$ 0.24 m), and 0.025 m in four rectangles going each positive and negative Cartesian direction with length 0.545 m and width 0.24 m (Figure 1). Outside of these areas the maximum edge is of 0.2 m and transition between each maximum edge size is made using a growth rate of 0.05 using NETGEN algorithm (Schöberl, 1997). The attributes of each mesh are presented in Table 3.

The number of points (computational cells) ranges from 33,049 to 25,960 from mesh A to mesh J. Grate A requires a finer discretization due to geometric constrains, and as such, the number of computational cells increase. On the other side, grate J is composed of a large open area which greatly reduces the number of computational points. This is visibly in Table 3 where the deviation from the average can be observed for the points, cells, and edges.

It is also observed in Table 3 that the deviations from the average for the cell areas and edge lengths are usually below 20%. This led us to accept the different grate meshes as equivalent given the physical constrains.

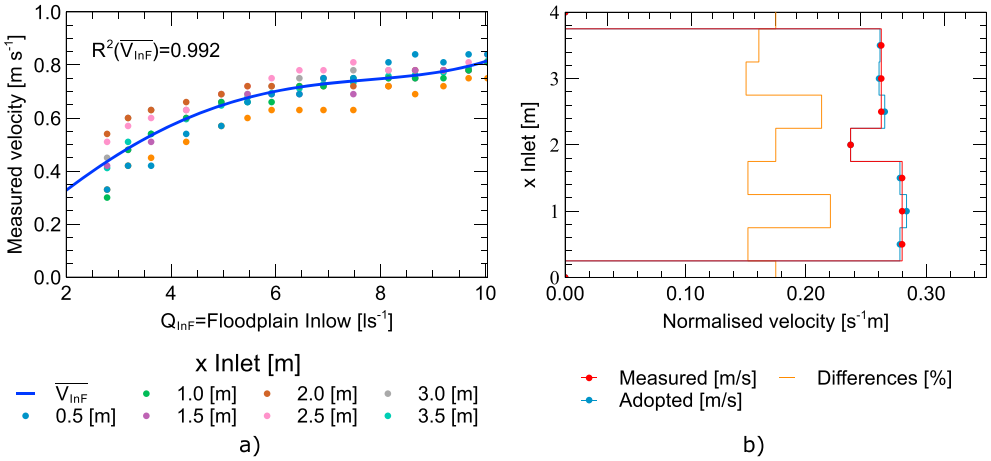

Figure 2. Inlet velocity boundary condition.

3. Results and Discussion

In the following, the experimental and numerical simulation results were compared in terms of (i) calculated flow through each grate inlet (i.e., exchange flow) and (ii) velocity fields within a 0.76 × 0.57-m area around the manhole grate. It should be noted that this comparison assumed that the surface velocities as recorded by the sPIV system are equivalent to depth-averaged velocities calculated by the model. Due to the relatively shallow flow depths under consideration, errors arising from this assumption are not expected to be significant.

3.1. Exchange Discharge

Numerical and experimental exchanged flow data for each test are presented in Figure 3. For each grate a linear trend was observed between experimental and numerical flow rates. The linear fit is represented by a solid line inside the simulated/measured area and as a dashed line outside. Trend coefficients are presented for each grate separately along with a global coefficient of determination.

Figure 3 shows that the experimentally exchanged flow values are almost always higher than numerical flows with differences between 0.16 and −0.05 L/s. The average difference is 9.2%. Grate-specific trend coefficients range from 1.034 to 1.178 with a global coefficient of 1.096. The variations between experimental and numerical are likely caused by the transition from weir-type flow to an orifice type (i.e., submerged) flow at the perimeter of the void spaces within the grates as the flow rises. The transition from weir type flow to an orifice type increases the local inflow in the experimental facility in most situations while the numerical model

Table 3
Numerical Mesh Dimensions

	Number			Edge length (m)			Cell area (m^2)		
Grate	Points	Cells	Edge	Minimum	Average	Maximum	Minimum	Average	Maximum
A	33,049	17,315	50,379	1.47E − 03	1.97E − 02	2.84E − 01	1.16E − 06	9.92E − 04	2.74E − 02
B	30,802	15,744	46,585	1.62E − 03	2.11E − 02	2.83E − 01	1.33E − 06	1.06E − 03	2.38E − 02
C	29,034	14,850	43,896	1.53E − 03	2.23E − 02	2.93E − 01	1.21E − 06	1.13E − 03	2.91E − 02
D	28,849	14,954	43,824	1.61E − 03	2.20E − 02	2.83E − 01	1.41E − 06	1.14E − 03	2.57E − 02
E	29,014	15,025	44,060	1.60E − 03	2.22E − 02	2.85E − 01	1.41E − 06	1.13E − 03	2.52E − 02
F	29,794	15,395	45,237	1.16E − 03	2.17E − 02	2.83E − 01	9.33E − 07	1.10E − 03	2.73E − 02
G	30,068	15,536	45,652	1.16E − 03	2.14E − 02	2.85E − 01	9.12E − 07	1.09E − 03	2.80E − 02
H	31,067	15,698	46,774	1.62E − 03	2.12E − 02	2.83E − 01	1.36E − 06	1.06E − 03	2.74E − 02
I	29,218	14,896	44,121	1.60E − 03	2.22E − 02	2.83E − 01	1.36E − 06	1.12E − 03	2.70E − 02
J	25,960	13,419	39,390	1.69E − 03	2.44E − 02	2.86E − 01	1.45E − 06	1.26E − 03	2.67E − 02
Average	29,685.5	15,283.2	44,991.8	1.51E − 03	2.18E − 02	2.85E − 01	1.25E − 06	1.11E − 03	2.68E − 02

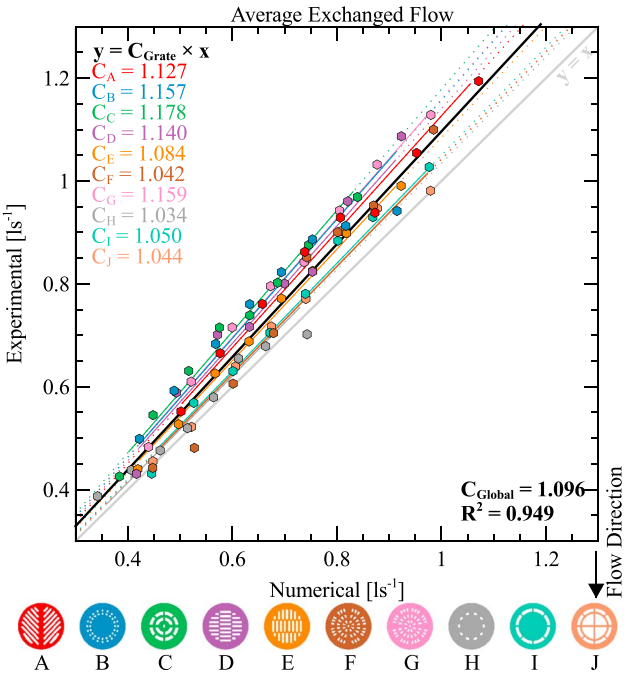

Figure 3. Comparison of experimental and numerical discharges for each grate and each flow.

cannot replicate the transition. Thus, a good numerical representation is expected in weir conditions, subject to an underprediction in exchange flow through the inner voids in each grate at higher flow rates. The magnitude of the transition from weir type flow to an orifice type seems to be dependent on the grate type. Grates I and J (with similar outside geometry) do not experience the transition as the weir perimeter is very similar while orifice conditions are not achieved. Grates I and J have relatively better agreement between numerical and experimental results (trend coefficients 1.04–1.05) while grates more prone to this effect, namely, A, B, and C, have a higher disparity (coefficient 1.27–1.78). Contradictory, grate H, which should also experience this transition, has the best agreement. This occurs because, both numerically and experimentally, the exchange flow is very small and therefore limited by the area of the void spaces in the grate and not the void perimeter. Grates D and E show that the orientation of the voids is important as the trend coefficients are different for the same static geometry but orientated in different directions. Overall, the comparison shows a close relationship between the numerical and the experimental data sets with some higher inflows in the experimental results due to a localized transition from weir to orifice conditions around the void areas of the grates, critical flow depth assumptions on the boundaries of the void, small variations in bed elevation, and/or inflow boundary conditions not fully reproduced in the numerical model.

3.2. Velocity Fields

The velocities near the manhole were analyzed in a rectangle 0.76 m long (1.225 to 1.987 m) and 0.57 m wide (1.755 to 2.325 m) for both the numerical and experimental data. Numerical data were interpolated to match exactly the experimental data points since the grid for the numerical data is finer than the experimental measurement grid. An example of flow vectors produced from the sPIV, numerical model, and the differences is presented in Figure 4 for grate type A and B for surface inflow rate of 9.29 and 6.33 L/s, respectively.

An overall comparison between the numerical and the experimental results was established for each velocity component and is shown in Figures 5 and 6 where experimental and numerical velocities at each experimental cell are plotted on the vertical and horizontal axes, respectively, for each grate and flow condition. Figure 5 shows the velocity for the longitudinal velocity component, while Figure 6 shows the correspondent transversal velocity component for all configurations tested and for all in flow conditions.

In the longitudinal direction (Figure 5), for the lower floodplain flows (4.27 to 6.33 L/s), the numerical model shows a tendency to produce lower velocities compared to the experimental data. This is consistent with the exchange flow values discussed above, as a higher longitudinal velocity usually implies a higher inflow to the manhole (unless the velocity is sufficient for the flow to pass directly over the grate). Grate H however has some higher velocities in the numerical simulation than the experimental data. This is due to a higher displacement to the left of the flow entry point due to the lack of capacity through the grate and as such an increase of the flow on the right side of the grate. This is visible in the experimental data; however, such a small detail is not visible in the numerical simulations. Another particular issue relates to the (almost) constant 0.2 s^{-1} m obtained in the numerical results for grates A–D that is not present in the experimental data. This occurs due to the transparent acrylic circumference of top of the manhole with the thickness of 0.075 m that was perceived by the sPIV as the same color of the particles and as such provided some inconsistent experimental data points in certain locations. Since this occurs upstream of the manhole inlet, where the velocity is relatively constant for the numerical model the result is a spread of experimental values (a horizontal band in Figure 4). For higher flows, the grates can be divided into four groups. The first, group 1, includes grates E, F, I, and J. This group shows very close patterns and a tendency to be fairly symmetrical in the $x = y$ line with a neglectable bias to the experimental or numerical velocities. The further the distance from the manhole center is, the closer the similarities between experimental and numerical results are. The second, group 2, includes grates A, B, C, and G. They show a fairly irregular distribution especially at points closer to the

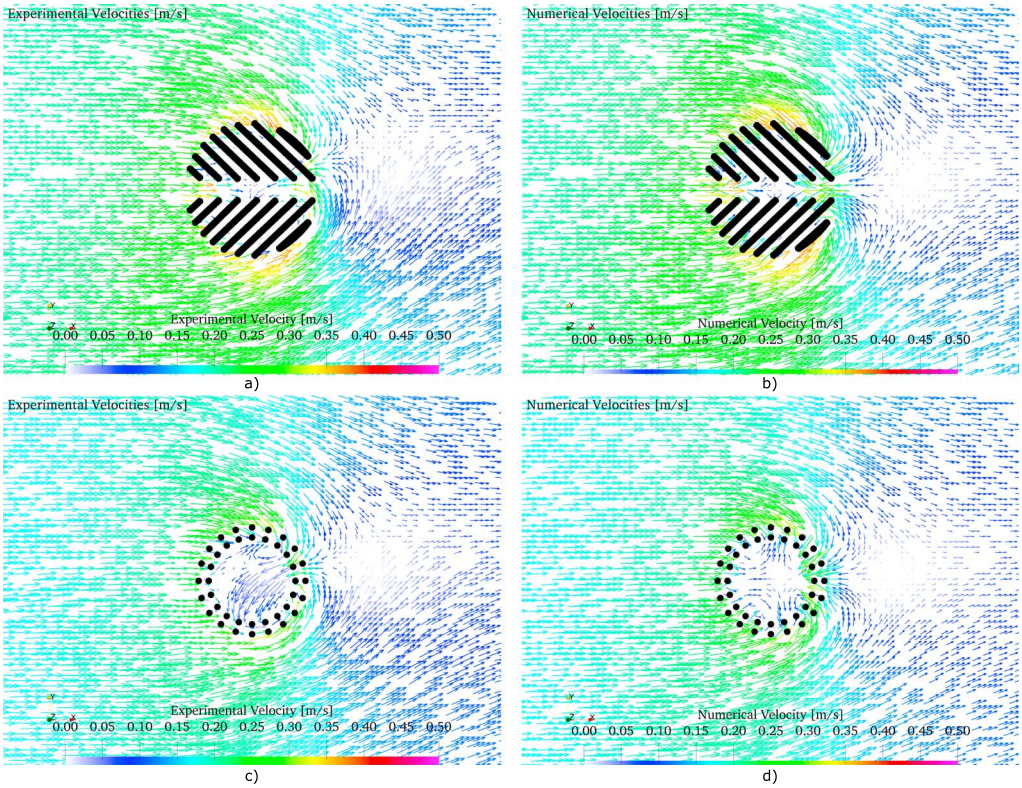

Figure 4. Velocity vectors for the numerical and experimental data (a) for grate and (b) for flow rate of 9.29 and 6.33 L/s.

manhole with a nonsymmetrical distribution when the flow increases. This phenomenon can be attributed to some small features of the flow, such as turbulence induced from the flow entering the manhole, transition from weir to orifice flow, or the nonsymmetrical nature of the inflow boundary conditions that are not captured by the numerical model because of its depth-averaged nature or upstream boundary approximations. The third, group 3, includes grate D and is completely biased toward the numerical underprediction due to the void area being larger in the longitudinal direction than the transversal direction. In this case the streamlines tend to reorientate around the voids such that flow enters the grate laterally and flows into the voids from both upstream and downstream directions. This phenomenon leaves a relatively narrow entrance hindering the flow through the void, which seems to result in highly 3-D flow and collision of both water veins. This results in the transition from weir to orifice at a relatively low flow rates for grate D. This could be overcome in the numerical model by introducing some restriction in the void boundary condition so that the flow could bypass over the first void spaces. However, this would require calibration and grate- and flow-specific experimental data, which is much more challenging to achieve. An alternative would be to compute the void spaces as cells and limit the inlet by the use of a weir or orifice coefficient. However, this approach would only be another simplification given that the velocity field in the voids is essentially 3-D, which is beyond the capacity of a 2-D depth-averaged representation of a SWE-based model. The fourth, group 4, includes grate H that has an inclined distribution due to the previously referred transition from weir to orifice and the very low grate capacity.

In the transversal direction (Figure 6), the global behavior of velocities follows a similar pattern to the longitudinal velocities. It is noticeable that globally the flow entering the manhole in the transverse direction has a higher velocity magnitude in the experimental data than in the numerical simulations. This is visible as most of the scatters tend to have an "*S*" or "8" shape with inception point at (0,0). It is also noteworthy that the results tend to be more concordant, the lower the magnitude of the velocities. This could be due to some small variations of the bed elevation that the numerical model does not take into account.

Lower flows show a fairly similar pattern between numerical and experimental results with little spread. For higher flows, all the comparisons seem to follow an approximate pattern with more or less "noise" or variation

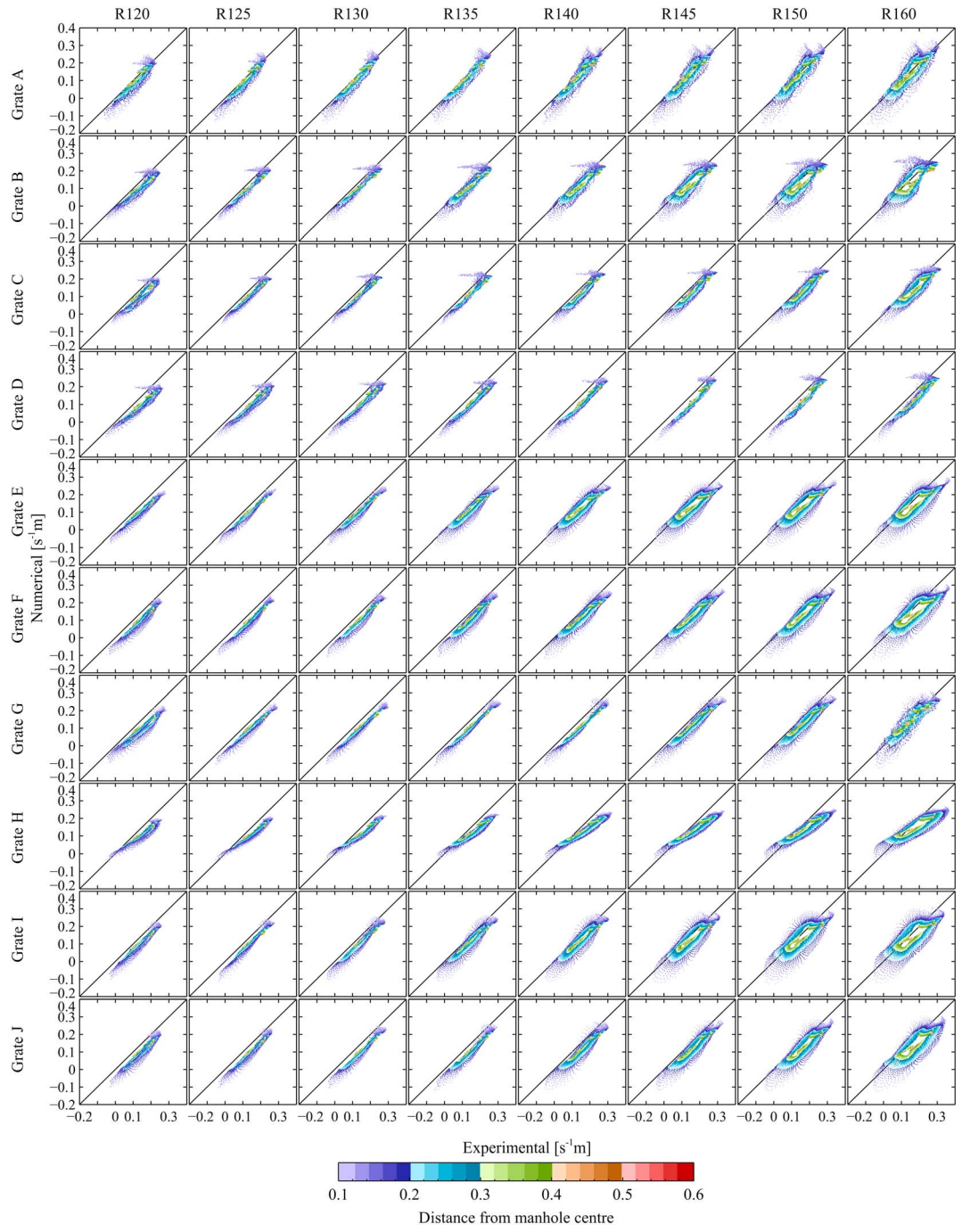

Figure 5. Comparison of experimental and numerical longitudinal velocities for all flows and all grates.

throughout the flows with the exceptions of grates B, D, and H. In grate D, the opposite behavior to that observed for the longitudinal velocities occurs (i.e., it shares the same effect as grate E in the longitudinal direction). The void spaces have a larger void distance in the transversal direction that limits the flow into the manhole structure. Grate B keeps the same irregularity as mentioned in the longitudinal direction with the same apparent justification: small features of the flow that the numerical model is unable to capture. Grate H, although very regular, still leans toward numerical underprediction, with higher experimental velocities. Once more, the further from the manhole, the more similarity between experimental and numerical velocities there is. Accurate characterization of the transversal and longitudinal void lengths (in

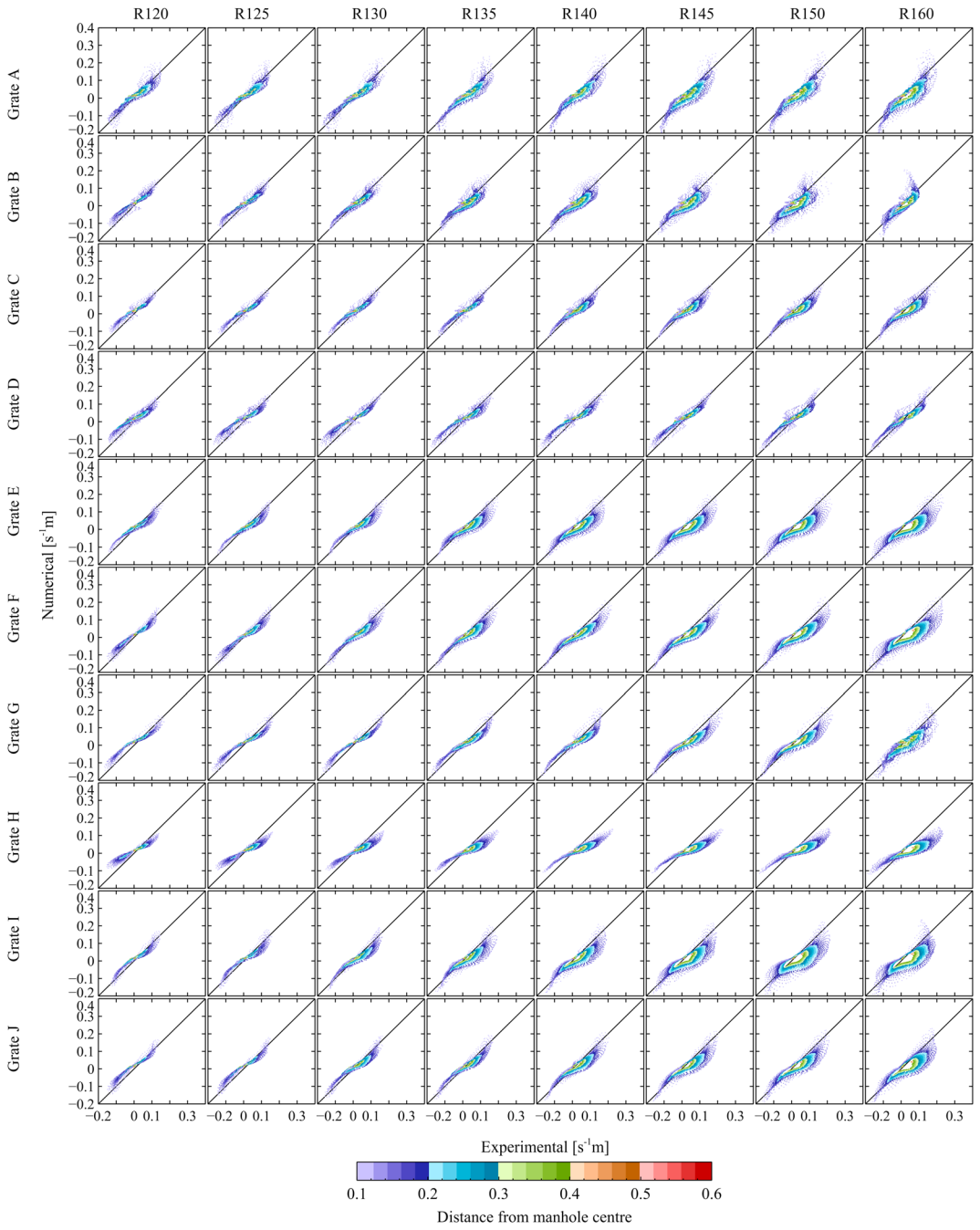

Figure 6. Comparison of experimental and numerical transverse velocities for all flows and all grates.

the inflow direction) are very important to get in order to get reasonable approximations from the numerical model. A longer void length in the longitudinal direction usually means a weir condition for the inflow, and as such, it is better represented by the numerical model.

The summary of the comparison between the numerical and experimental velocities for all flow conditions and grate types is plotted in Figure 7.

Figure 7a (left) shows the summary of the results for the velocity in the longitudinal direction, while Figure 7b compares experimental and numerical data for the velocity in the transversal direction. Two histograms for the velocity densities are presented for both the numerical (blue) and the experimental (orange) with

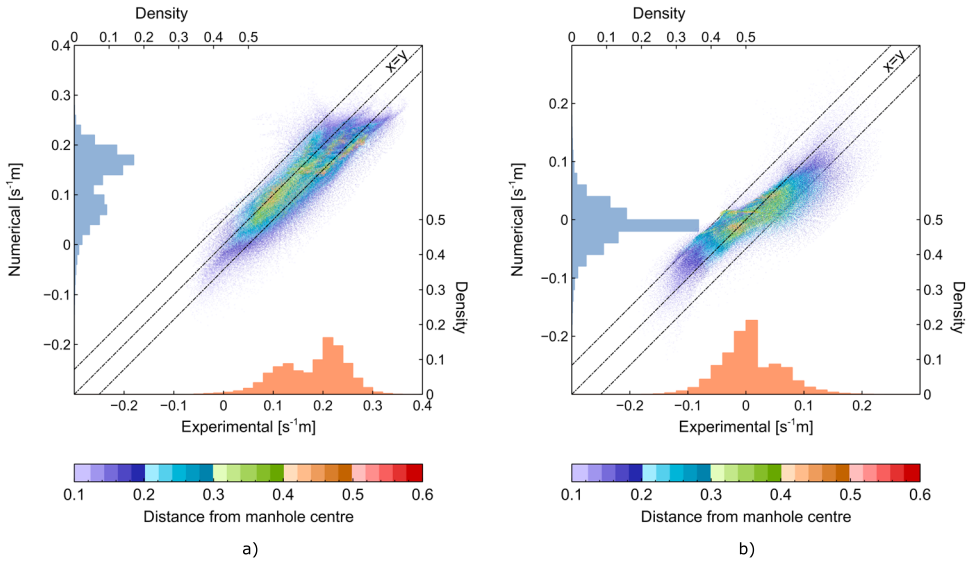

Figure 7. Velocity comparison in the (a) longitudinal and (b) transversal direction with the respective velocity densities (histograms).

density axis on the horizontal top and vertical right, respectively. Three lines divide the plot being $x = y$ and two lines to bound the difference between experimental and numerical to -0.05 or 0.05 s^{-1} m.

Figure 8 presents the results as a histogram of the numerical density of deviation from the experimental results for each velocity component. Globally, it is visible that the longitudinal velocities have a more consistent distribution with a fairly large amount (96%) of points being within the 0.05-s^{-1} m difference range (Figure 8a). There is a noteworthy inclination toward higher experimental velocities as shown with 86% of the velocity points. This is also visible in Figure 7a as the majority of the points are beneath the $x = y$ line. For the transversal velocities, the numerical velocities are on average higher while the experimental are more scattered. When comparing the velocity histograms for the experimental and numerical in the longitudinal direction (Figure 7a), they have a similar shape which points to a good relation between experimental and numerical results. For the transversal direction, the shape is inclined toward the numerical model, with the difference as a result of small differences in the flow that change the direction in the experimental but are concentrated at approximately 0 s^{-1} m in the numerical model (Figure 7a).

It is noticed that a large majority of the differences are within a range of 0.05 s^{-1} m. The last analysis establishes a degree of correlation between each numerical and experimental data set for the velocity magnitude

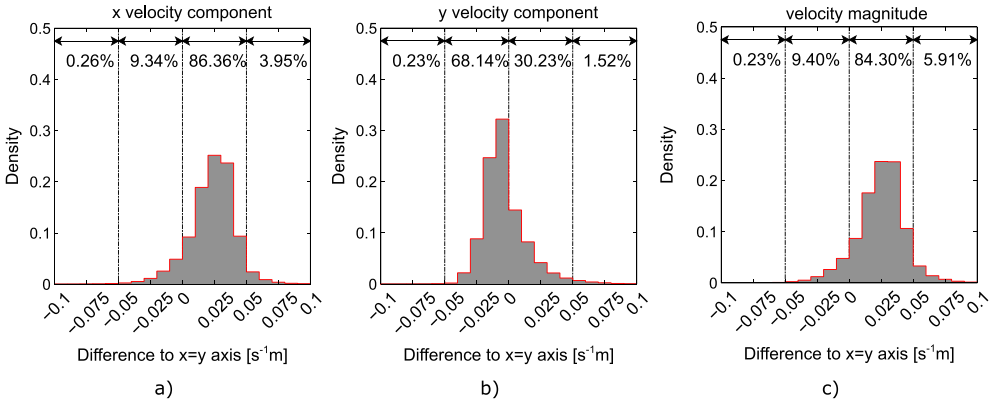

Figure 8. Numerical density of deviation from the experimental results.

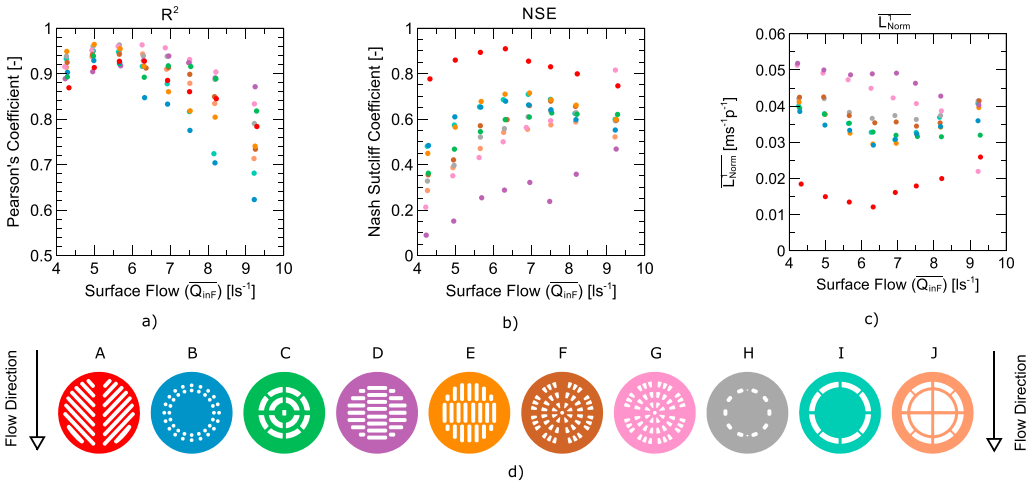

Figure 9. Correlation coefficients. (a) Pearson. (b) NSE. (c) Average deviation.

$U = \sqrt{u^2 + v^2}$. Four correlation parameters (Pearson's coefficient (8) (Rodgers & Nicewander, 1988), Nash-Sutcliff coefficient (9) (Nash & Sutcliffe, 1970), and the $\overline{L^1_{Norm}}$(10) (Horn & Johnson, 1990)) were used in order to provide the widest possible comparison for each flow and each grate.

$$R^2 = \left[\frac{\Sigma_{i=1}^{n}\left(U_i^E - \overline{U^E}\right)\left(U_i^N - \overline{U^N}\right)}{\sqrt{\Sigma_{i=1}^{n}\left(U_i^E - \overline{U^E}\right)^2\left(U_i^N - \overline{U^N}\right)^2}}\right]^2 \tag{8}$$

$$\mathrm{NSE} = 1 - \frac{\Sigma_{i=1}^{n}\left(U_i^N - U_i^E\right)^2}{\Sigma_{i=1}^{n}\left(U_i^E - \overline{U^E}\right)^2} \tag{9}$$

$$\overline{L^1_{\mathrm{Norm}}} = \frac{\Sigma_{i=1}^{n}\left(U_i^E - U_i^B\right)}{n} \tag{10}$$

Figure 9 shows the coefficients plotted against the surface inflow (Q_{InF}).

Pearson's coefficient is the centered and standardized sum of cross product of two models; as such, it shows if two sets are linearly correlated. As seen in Figure 9, the experimental and numerical data show a good agreement for all grates up to 7-L/s surface inflow. After 7 L/s, grates A, C, D, G, and H still show a good agreement (>0.75) with E, F, and J within reasonable agreement values (>0.7). Grates B and I have the lowest correlation between the numerical and the experimental (>0.6). This does not mean that the results are much worse; however, it implies that the relation deviates from the linearity between experimental and numerical possibly due to the physical nonlinear effects not captured by the numerical model. Averaging all the flows, the lowest correlation is of 0.82 for grate B and the best is for grate G with 0.93, which shows that globally there is a good agreement with local discrepancies.

NSE (Figure 9, center) determines the relative magnitude of the simulated variance compared to the measured variance. Globally, grate A shows the best results with an average of 0.83 while the worst result is for grate D with a somewhat poor result of 0.27. This is due to the aforementioned experimental velocity reduction just upstream of the manhole that results in a constant line in the longitudinal velocity as seen in Figure 5. To add to this there is a bias toward higher experimental velocities that is noteworthy in NSE. In fact, NSE, in this study, shows mainly the deviation and not the correlation from $x = y$ which explains the results obtained.

From a more physical perspective we also calculated the average deviation (Figure 9c) for each model and each flow ($\overline{L^1_{\mathrm{Norm}}}$). Grate A has an average deviation of 0.017 and 0.012 s^{-1} m as the minimum. Grates B, C,

E, I, F, and H have higher deviations up to 0.04 s^{-1} m and grates J, G, and D up to 0.05 s^{-1} m showing a larger spread of the results. The results show that globally all the average deviations are below 0.05 s^{-1} m.

4. Conclusions

In this study an extensive comparison between experimentally observed and numerically simulated drainage flows through a range of ten grate inlet designs has been presented under subcritical flow conditions. Novel velocity field data sets were collected using a sPIV system which enabled flow characteristics to be compared in terms of both drainage flow rates and 2-D velocity field in the vicinity of the manhole structure. This allows a closer critical examination of model performance. Based on the use of a 2-D numerical scheme using a generic critical depth boundary condition to represent drainage flows, it was shown that good level of agreement between the experimental and numerical inflows could be achieved. Experimentally measured and numerically modeled inflows were found to have an average global difference of 9.2%. It was verified that the further from the manhole, the closer (more similar) the measured and simulated velocities are, due mainly to the more directional flow. A variation in overall model performance was noted to be dependent on both the geometrical properties of the grate and the flow rate. Grates with a relatively high void perimeter at the edge of the grate, or those which transfer from weir inflow to orifice inflow conditions at a lower flow rate, lead to higher levels of numerical underprediction at higher flow rates, as the critical depth boundary condition does not fully capture inflow through the void spaces at the center of the grate structure. Appropriate characterization of transversal and longitudinal void lengths (i.e., in the inflow direction) within numerical schemes are important to get accurate modeling representations as void lengths generally determine the transition point from weir to orifice conditions.

Overall, the study demonstrates the potential for 2-D models to represent drainage inlet flows within urban flood modeling tools. As urban overland flow models are commonly simulated by 2-D schemes, this provides improved future model integration options when compared with 3-D models of urban drainage structures which have been previously studied. In the shorter term, the study also demonstrates the potential for the use of 2-D models for other applications, such as effective inlet grate design, or to derive energy loss coefficients for a range of inlet types for use within existing weir/orifice type surface/sewer relationships, hence reducing reliance on model calibration or the use of physical modeling studies. This may be particularly useful in low-depth conditions, when accurately measuring the effective wetted perimeter, void area, and local hydraulic head within the grates is challenging. Further work is required to consider the validity of numerical modeling tools under a greater range of flow conditions (i.e., supercritical flow).

Acknowledgments
No potential conflict of interest was reported by the authors. The research was supported by the UK Engineering and Physical Sciences Research Council (EP/K040405/1). Experimental data supporting the conclusions can be obtained as supporting information at https://www.sheffield.ac.uk/floodinteract.

References

Bock, P., Li, W. H., & Geyer, J. C. (1956). Hydraulic behavior of storm-water inlets: V. A simplified method of determining capacities of single and multiple inlets. *Sewage and Industrial Wastes*, *28*(6), 774–784.

Brufau, P., & García-Navarro, P. (2000). Two-dimensional dam break flow simulation. *International Journal for Numerical Methods in Fluids*, *33*(1), 35–57. https://doi.org/10.1002/(SICI)1097-0363(20000515)33:1<35::AID-FLD999>3.0.CO;2-D

Carmer, C., Rummel, A., & Jirka, G. (2009). Mass transport in shallow turbulent wake flow by planar concentration analysis technique. *Journal of Hydraulic Engineering*, *135*(4), 257–270. https://doi.org/10.1061/(ASCE)0733-9429(2009)135:4(257)

Cea, L., Legout, C., Darboux, F., Esteves, M., & Nord, G. (2014). Experimental validation of a 2D overland flow model using high resolution water depth and velocity data. *Journal of Hydrology*, *513*, 142–153. https://doi.org/10.1016/j.jhydrol.2014.03.052

Chertock, A., Cui, S., Urganov, A., & Wu, T. (2015). Well-balanced positivity preserving central-upwind scheme for the shallow water system with friction terms. *International Journal for Numerical Methods in Fluids*, *78*(6), 355–383. https://doi.org/10.1002/fld.4023

DEFRA (2011). *Annex B: National Built Standards, Design and Construction of new gravity fould sewers and lateral drains, Water Industry Act 1991 Section 106B, Flood and Water Management Act 2010 Section 42*. London: DEFRA Publications. Retrieved from https://www.gov.uk/government/uploads/system/uploads/attachment_data/file/82516/new-build-sewers-consult-annexb-sos-standards-111220.pdf

Djordjevic, S., Saul, A. J., Tabor, G. R., Blanksby, J., Galambos, I., Sabtu, N., & Sailor, G. (2013). Experimental and numerical investigation of interactions between above and below ground drainage systems. *Water Science and Technology*, *67*(3), 535–542. https://doi.org/10.2166/wst.2012.570

Gómez, M., & Russo, B. (2005). Comparative study of methodologies determine inlet efficiency from test data. HEC-12 methodology vs UPC method. *Water Resources Management*, *80*, 623–632. https://doi.org/10.2495/WRM050621

Gómez, M., & Russo, B. (2007). Hydraulic efficiency of macro-inlets. *Novatech*, 1157–1164.

Gómez, M., & Russo, B. (2009). Hydraulic efficiency of continuous transverse grates for paved areas, (April), 225–230.

Gómez, M., & Russo, B. (2011). Methodology to estimate hydraulic efficiency of drain inlets. *Proceedings of the Institution of Civil Engineers: Water Management*, *164*(2), 81–90. https://doi.org/10.1680/wama.900070

Horn, R. A., & Johnson, C. R. (1990). *Matrix Analysis*. Cambridge, England: Cambridge University Press.

Leandro, J., Lopes, P., Carvalho, R., Páscoa, P., Martins, R., & Romagnoli, M. (2014). Numerical and experimental characterization of the 2D vertical average-velocity plane at the center-profile and qualitative air entrainment inside a gully for drainage and reverse flow. *Computers and Fluids*, *102*, 52–61. https://doi.org/10.1016/j.compfluid.2014.05.032

Li, W. H., Geyer, J. C., & Benton, G. S. (1951). Hydraulic behavior of storm-water inlets: I. Flow into gutter inlets in a straight gutter without depression. *Sewage and Industrial Wastes*, *23*(1), 34–46.
Li, W. H., Goodell, B. C., & Geyer, J. C. (1954a). Hydraulic behavior of storm-water inlets: III. Flow into deflector inlets. *Sewage and Industrial Wastes*, *26*(7), 836–842. Retrieved from doi:https://doi.org/10.2307/25032515
Li, W. H., Goodell, B. C., & Geyer, J. C. (1954b). Hydraulic behavior of storm-water inlets: IV. Flow into depressed combination inlets. *Sewage and Industrial Wastes*, *26*(8), 967–975.
Li, W. H., Sorteberg, K. K., & Geyer, J. C. (1951). Hydraulic behavior of storm-water inlets: II. Flow into curb-opening inlets. *Sewage and Industrial Wastes*, *23*(6), 722–738.
Lopes, P., Leandro, J., Carvalho, R. F., Russo, B., & Gómez, M. (2016). Assessment of the ability of a volume of fluid model to reproduce the efficiency of a continuous transverse gully with grate. *Journal of Irrigation and Drainage Engineering*, *142*(10). 04016039. https://doi.org/10.1061/(ASCE)IR.1943-4774.0001058
Lopes, P., Leandro, J., Carvalho, R. F. F., Páscoa, P., & Martins, R. (2015). Numerical and experimental investigation of a gully under surcharge conditions. *Urban Water Journal*, *12*(6), 468–476. https://doi.org/10.1080/1573062X.2013.831916
Martins, R., Kesserwani, G., Rubinato, M., Lee, S., Leandro, J., Djordjević, S., & Shucksmith, J. D. (2017). Validation of 2D shock capturing flood models around a surcharging manhole. *Urban Water Journal*, *14*(9), 892–899. https://doi.org/10.1080/1573062X.2017.1279193
Martins, R., Leandro, J., & Carvalho, R. F. (2014). Characterization of the hydraulic performance of a gully under drainage conditions. *Water Science and Technology*, *69*(12), 2423–2430. https://doi.org/10.2166/wst.2014.168
Martins, R., Leandro, J., Chen, A. S., & Djordjević, S. (2017). A comparison of three dual drainage models: Shallow water vs local inertial vs diffusive wave. *Journal of Hydroinformatics*, *19*(3), 331–348. https://doi.org/10.2166/hydro.2017.075
Martins, R., Leandro, J., & Djordjević, S. (2015). A well balanced roe scheme for the local inertial equations with an unstructured mesh. *Advances in Water Resources*, *83*, 351–363. https://doi.org/10.1016/j.advwatres.2015.07.007
Martins, R., Leandro, J., & Djordjevic, S. (2017). Wetting and drying numerical treatments for the roe Riemann scheme. *Journal of Hydraulic Research*, *56*(2), 256–267. https://doi.org/10.1080/00221686.2017.1289256
Molls, T., Zhao, G., & Molls, F. (1998). Friction slope in depth-averaged flow. *Journal of Hydraulic Engineering*, *125*(5), 549–585. https://doi.org/10.1061/(ASCE)0733-9429(1999)125:5(549)
Nasello, C., & Tucciarelli, T. (2005). Dual multilevel urban drainage model. *Journal of Hydraulic Engineering*, *131*(9), 748–754. https://doi.org/10.1061/(Asce)0733-9429(2005)131:9(748)
Nash, J. E., & Sutcliffe, J. V. (1970). River flow forecasting through conceptual models: Part I—A discussion of principles. *Journal of Hydrology*, *10*(3), 282–290. https://doi.org/10.1016/0022-1694(70)90255-6
Odzemir, H., Sampson, C. C., de Almeida, G. A. M., & Bates, P. D. (2013). Evaluating scale and roughness effects in urban flood modelling using terrestrial LIDAR data. *Hydrology and Earth System Sciences*, *14*, 4015–4030.
Rodgers, J. L., & Nicewander, W. A. (1988). Thirteen ways to look at the correlation coefficient. *The American Statistician*, *42*(1), 59–66. https://doi.org/10.1080/00031305.1988.10475524
Rubinato, M. (2015). Physical scale modelling of urban flood systems, (PhD thesis). The University of Sheffield, 2015. Retrieved from http://etheses.whiterose.ac.uk/id/eprint/9270
Rubinato, M., Lee, S., Martins, R., & Shucksmith, J. D. (2018). Surface to sewer flow exchange through circular inlets during urban flood conditions. *Journal of Hydroinformatics*, *20*(3), 564–576. https://doi.org/10.2166/hydro.2018.127
Rubinato, M., Martins, R., Kesserwani, G., Leandro, J., Djordjević, S., & Shucksmith, J. (2017). Experimental calibration and validation of sewer/surface flow exchange equations in steady and unsteady flow conditions. *Journal of Hydrology*, *552*, 421–432. https://doi.org/10.1016/j.jhydrol.2017.06.024
Russo, B., Gómez, M., & Tellez, J. (2013). Methodology to estimate the hydraulic efficiency of nontested continuous transverse grates. *Journal of Irrigation and Drainage Engineering*, *139*(10), 864–871. https://doi.org/10.1061/(ASCE)IR.1943-4774.0000625
Schöberl, J. (1997). NETGEN an advancing front 2D/3D-mesh generator based on abstract rules. *Computing and Visualization in Science*, *1*(1), 41–52. https://doi.org/10.1007/s007910050004
Song, L., Zhou, J., Guo, J., Zou, Q., & Liu, Y. (2011). A robust well-balanced finite volume model for shallow water flows with wetting and drying over ir regular terrain. *Advances in Water Resources*, *34*(7), 915–932. https://doi.org/10.1016/j.advwatres.2011.04.017
Spaliviero, F., May, R. W. P., & Escarameia, M. (2000). Spacing of road gullies. Hydraulic performance of BS EN 124 gully gratings. HR Walingford, 44(0).
Tracy, H. J. (1957). Discharge characteristics of broad-crested weirs, Geological Survey Circular 397, Washington, DC.
Weitbrecht, V., Khn, G., & Jirka, G. H. (2002). Large scale PIV-measurements at the surface of shallow water flows. *Journal of Flow Measurement and Instrumentation*, *13*(5-6), 237–245. https://doi.org/10.1016/S0955-5986(02)00059-6
Yang, L., Smith, J. A., Baeck, M. L., & Zhang, Y. (2016). Flash flooding in small urban watersheds: Storm event hydrologic response. *Water Resources Research*, *52*, 4571–4589. https://doi.org/10.1002/2015WR018326
Yang, S., Paik, K., McGrath, G. S., Urich, C., Krueger, E., Kumar, P., & Rao, P. S. C. (2017). Functional topology of evolving urban drainage networks. *Water Resources Research*, *53*, 8966–8979. https://doi.org/10.1002/2017WR021555